
Sparse Dynamic Distribution Decomposition: Efficient Integration of Trajectory and Snapshot Time Series Data

Jake P. Taylor-King
Relation Therapeutics
jake@relationrx.com

Cristian Regep
Relation Therapeutics
cristian@relationrx.com

Jyothish Soman
Relation Therapeutics
jyothish@relationrx.com

Flawnson Tong
Relation Therapeutics
flawnson1@gmail.com

Catalina Cangea
Relation Therapeutics
catalina.cangea@gmail.com

Charlie Roberts
Relation Therapeutics
charlie@relationrx.com

Abstract

Dynamic Distribution Decomposition (DDD) was introduced in Taylor-King *et al.* [30] as a variation on Dynamic Mode Decomposition. In brief, by using basis functions over a continuous state space, DDD allows for the fitting of continuous-time Markov chains over these basis functions and as a result continuously maps between distributions. The number of parameters in DDD scales by the square of the number of basis functions; we reformulate the problem and restrict the method to compact basis functions which leads to the inference of sparse matrices only — hence reducing the number of parameters. Finally, we demonstrate how DDD is suitable to integrate both trajectory time series (paired between subsequent time points) and snapshot time series (unpaired time points). Methods capable of integrating both scenarios are particularly relevant for the analysis of biomedical data, whereby studies observe population at fixed time points (snapshots) and individual patient journeys with repeated follow ups (trajectories).

Code to be made available at: <https://github.com/RelationRx/SparseDDD>

1 Introduction

Consider two scenarios, the first whereby a set of (stochastic) sample path trajectories are observed

$$\mathcal{T} = \left\{ \mathbf{X}_k(t_r) \in \mathbb{R}^d : \mathbf{X}_k(t_r) = \mathbf{X}_k(t_{r-1}) + \int_{t_{r-1}}^{t_r} \mathbf{f}(\mathbf{X}_k(s))dY(s) \text{ for } \begin{array}{l} r = 1, \dots, R_{\mathcal{T}} \\ k = 1, \dots, K_{\mathcal{T}} \end{array} \right\}, \quad (1)$$

and the second where snapshots are reported at fixed points in time from the same initial state

$$\mathcal{S} = \left\{ \mathbf{X}_{k_r}(t_r) \in \mathbb{R}^d : \mathbf{X}_{k_r}(t_r) = \mathbf{X}_{k_r}(t_0) + \int_{t_0}^{t_r} \mathbf{f}(\mathbf{X}_{k_r}(s))dY(s) \text{ for } \begin{array}{l} r = 1, \dots, R_{\mathcal{S}} \\ k_r \in \mathbb{N}_+ \end{array} \right\}. \quad (2)$$

In equations (1)–(2), the integrals are over a suitable class of random process, e.g., a pathwise Stieltjes integral for Hölder continuous random processes $\mathbf{X}(t)$ and $Y(t)$ [4]. For simplicity, a stochastic

differential equation (SDE) model would suffice — although the methodology presented applies to more general stochastic processes. We present a method to integrate both \mathcal{T} and \mathcal{S} for a predictive time series model.

The ability to integrate different sources and formats of temporal data is hugely important to the biomedical community. For a topical example, early data from patients with COVID-19 infections has led to the single cell characterisation [29] of various tissues at different stages (and outcomes) during infection, such as healthy (susceptible), early infection, the pulmonary phase, the hyper-inflammatory phase and finally leading to: a healthy (recovered) state, a fibrotic state, or even death [28]. However these are *not* the same patients being followed longitudinally — only recently has data started to become available for the monitoring of individual patient journeys [36]. While there may have been differences in the collection, preprocessing and quality control protocols that need addressing, hypothetically said datasets should be combined such that the resulting analysis leads to higher quality inferences than any one dataset alone.

In experimental and clinical settings, discrete-time models, such as Dynamic Mode Decomposition (DMD) [31, 33, 25], are unsuitable for the unequally spaced observations that typically occur in real world experimental scenarios [6]. Countless methods for time series analysis have been developed for trajectory data, often based on mechanical or phenomenological ODE [1, 34, 22] or SDE [18, 8] models in various scenarios, e.g., patient data [2] or signalling networks [35]. Methods for snapshot time series are a more recent phenomenon due to the wide availability of “*omic*” data that typically requires a destructive measurement process [38]. These methods involve mapping distributions between time points, for example via minimising earth mover’s distance between subsequent time points [24], or inferring a potential well [11]. To clarify terminology, *pseudotime methods* for inferring trajectories of differentiating cells within a heterogeneous population for a single snapshot exist [27, 5, 23, 3]. Finally, in the work by Weinreb *et al.* [32], it is shown there are limits on what may be inferred from snapshot data alone — there are too many models that are hypothetically possible. Therefore, we posit that approaches integrating both trajectory and snapshot data (when available) should be utilised.

In this work, we propose a sparsity-promoting modification on Dynamic Distribution Decomposition (DDD) [30] — itself an extension to DMD. DMD and related approaches are emerging powerful methods for (often discrete) time series analysis capable of various tasks: analysis of key behaviours [26], anomaly/error detection [30], control [17], parameter estimation [19, 21] and scaling into high dimensions [16]. DDD is essentially the numerical approximation of the Perron–Frobenius operator [15, 14] in continuous time, with constraints to enforce positivity and conservation of mass. In contrast, DMD approximates the Koopman operator. In more general terms, DDD fits a continuous-time Markov chain over a set of basis functions, thus learning an autonomous dynamical system. This approach is highly general and does not distinguish between trajectory and snapshot datasets. However, the Markov rate matrix is dense and therefore computationally expensive to infer for a large number of basis functions. We show that by limiting the behaviour of the Perron–Frobenius operator to local differential operators only, we can recast the problem such that one only has to infer a sparse matrix.

In Section 2, we present the method for both DDD and Sparse DDD. In Section 3, we apply the method to a synthetic dataset generated by an SDE and show that we can integrate a small snapshot dataset with a small trajectory dataset and obtain reduced errors below either dataset alone. Finally, we provide a discussion of the methodological advantages and disadvantages in Section 4.

2 Method

One of the most general mathematical set ups for modelling the evolution of a probability density involves the specification of a hyperbolic (transport) or parabolic partial differential equation and then solving forward in time. The most general of such equations involves the Perron–Frobenius operator \mathcal{P} (in continuous time)

$$\frac{\partial}{\partial t} \varrho(t, \mathbf{x}) = \mathcal{P} \varrho(t, \mathbf{x}), \quad (3)$$

with constraints $\int_{\mathcal{M}} \varrho(t, \mathbf{x}) d\mathbf{x} = 1$ and $\varrho(t, \mathbf{x}) \geq 0$ and initial condition $\varrho(t = 0, \mathbf{x}) = \varrho_0(\mathbf{x})$. Said operators can account for many dynamical systems — see examples.

Example 1: Stochastic Matrices as Perron–Frobenius Operators

Consider a discrete-time Markov chain over a countable number of discrete states $i \in \mathcal{I} \subset \mathbb{Z}$ with recursive relation

$$c_i^{(k+1)} = \sum_{j \in \mathcal{I}} P_{ij} c_j^{(k)}, \quad k = 0, 1, 2, \dots, \quad (4)$$

then P_{ij} is a left stochastic matrix with $P_{ij} = \Pr(X_{k+1} = i | X_k = j)$ and $\sum_{i \in \mathcal{I}} P_{ij} = 1$. In this case, P is the Perron–Frobenius operator.

Example 2: Fokker–Planck Equations as Perron–Frobenius Operators

As an alternative, consider continuous-time stochastic differential equation $\{\mathbf{X}_t \in \mathbb{R}^d : t \geq 0\}$

$$d\mathbf{X}_t = \boldsymbol{\mu}(\mathbf{X}_t, t) dt + \boldsymbol{\sigma}(\mathbf{X}_t, t) d\mathbf{W}_t, \quad (5)$$

for $\boldsymbol{\mu} \in \mathbb{R}^d$ and $\boldsymbol{\sigma}(\mathbf{X}_t, t) \in \mathbb{R}^{d \times d'}$ where \mathbf{W}_t is a d' -dimensional standard Wiener process. By defining diffusion tensor $\mathbf{D} = \frac{1}{2} \boldsymbol{\sigma} \boldsymbol{\sigma}^\top$, we write the Fokker–Planck equation, a partial differential equation for the probability density $\varrho(t, \mathbf{x})$ that $\mathbf{X}_t \in [\mathbf{x}, \mathbf{x} + \Delta \mathbf{x}]$ as

$$\frac{\partial \varrho(\mathbf{x}, t)}{\partial t} = - \sum_{i=1}^d \frac{\partial}{\partial x_i} [\mu_i(\mathbf{x}, t) \varrho(\mathbf{x}, t)] + \sum_{i=1}^d \sum_{j=1}^d \frac{\partial^2}{\partial x_i \partial x_j} [D_{ij}(\mathbf{x}, t) \varrho(\mathbf{x}, t)]. \quad (6)$$

By comparing equation (3) to equation (6), we see that the right hand side to the Fokker–Planck equation is the Perron–Frobenius operator.

Link to transition kernel Finally, we can build intuition for operator \mathcal{P} by linking kernel function $k_t(\mathbf{x}, \mathbf{y}) = \Pr(\mathbf{X}_t = \mathbf{x} | \mathbf{X}_0 = \mathbf{y})$ to the exponentiated operator via the equation

$$e^{t\mathcal{P}} \varrho_0(\mathbf{x}) = \int_{\mathcal{M}} k_t(\mathbf{x}, \mathbf{y}) \varrho_0(\mathbf{y}) d\mathbf{y}. \quad (7)$$

2.1 Finite Dimensional Approximation

We need to find a finite dimensional approximation of \mathcal{P} ; we achieve this via non-negative basis functions $\boldsymbol{\psi}(\mathbf{x}) = [\psi_1(\mathbf{x}), \dots, \psi_N(\mathbf{x})]^\top$ that we specify as probability density functions; whereby $\int_{\mathcal{M}} \psi_j(\mathbf{x}) d\mathbf{x} = 1$. For all $t \in (t_1, t_R)$ we take the ansatz that we can expand ϱ as a Galerkin approximation

$$\tilde{\varrho}(t, \mathbf{x}) = \mathbf{c}^\top(t) \boldsymbol{\psi}(\mathbf{x}) = \sum_{j=1}^N c_j(t) \psi_j(\mathbf{x}), \quad (8)$$

where $\mathbf{c}(t) = [c_1(t), \dots, c_N(t)]^\top$. For conservation of mass we require $\sum_{i=1}^N c_i(t) = 1$. A tilde (\sim) over ϱ denotes when this approximation is used.

We then derive a linear system of ODEs for the coefficients $\mathbf{c}(t)$ by noting in weak form [37, 10] equation (3) is

$$\langle \psi_i, \dot{\varrho} \rangle_\mu = \langle \psi_i, \mathcal{P} \varrho \rangle_\mu \quad \text{for} \quad \langle f, g \rangle_\mu = \int_{\mathcal{M}} f(\mathbf{x}) g(\mathbf{x}) d\mu(\mathbf{x}), \quad (9)$$

and therefore

$$M \dot{\mathbf{c}}(t) = Q \mathbf{c}(t) \quad \text{for} \quad \begin{aligned} M_{ij} &= \langle \psi_i, \psi_j \rangle_\mu \\ Q_{ij} &= \langle \psi_i, \mathcal{P} \psi_j \rangle_\mu. \end{aligned} \quad (10)$$

2.2 Construction of Loss Function

We now motivate a choice in loss function analogous to least squares fitting error for ODEs. Assuming that M is invertable, then we define the projection of \mathcal{P} onto the basis functions as

$$P := M^{-1} Q. \quad (12)$$

Calculation of Galerkin Approximation Coefficients for PDFs

When basis functions are probability density functions, we can find the values of c_r at each time point by noting that the value of $c_j(t_r)$ must be proportional to the probability that basis function j created the data at that time point, therefore

$$c_j(t_r) = \sum_{i=1}^{n_r} \psi_j(\mathbf{x}_{r,i}) / \sum_{j=1}^N \sum_{i=1}^{n_r} \psi_j(\mathbf{x}_{r,i}). \quad (11)$$

We can solve the system of ODES in equation (10) via the matrix exponential operation, specifically

$$\mathbf{c}(t) = e^{tP} \mathbf{c}_*, \quad (13)$$

where \mathbf{c}_* are the coefficients at corresponding to the initial condition $\tilde{\varrho}_0 = \mathbf{c}_*^\top \psi(\mathbf{x})$. In equation (13), we allow mis-specification of the initial condition $\varrho_0 = \varrho_0(\mathbf{x})$ by specifying that \mathbf{c}_* are free parameters within model. We can use the L^2 norm to give a measure of how well \mathcal{P} represents the evolution of the densities. The squared relative prediction error at time $t = t_r$ for $r = 0, \dots, R$ is

$$\epsilon_r^2(\mathcal{P}, \varrho_0) := \frac{\|e^{t_r \mathcal{P}} \varrho_0(\cdot) - \varrho(t_r, \cdot)\|_{L^2}^2}{\|\varrho(t_r, \cdot)\|_{L^2}^2} = \frac{\int_{\mathcal{M}} [e^{t_r \mathcal{P}} \varrho_0(\mathbf{x}) - \varrho(t_r, \mathbf{x})]^2 d\mathbf{x}}{\int_{\mathcal{M}} [\varrho(t_r, \mathbf{x})]^2 d\mathbf{x}}. \quad (14)$$

We then define the mean squared relative prediction error as $\sum_{r=0}^R \epsilon_r^2(\mathcal{P}, \varrho_0) / (R + 1)$. Were this computationally possible, we would like to infer the differential operator and initial state

$$\{\mathcal{P}, \varrho_0\} := \arg \min_{\mathcal{P}, \varrho_0 \geq 0, \varrho_0 \in L^1} \frac{1}{R + 1} \sum_{r=0}^R \epsilon_r^2(\mathcal{P}, \varrho_0). \quad (15)$$

However, we must use the finite dimensional Galerkin approximation; therefore we approximate

$$\epsilon_r^2(\mathcal{P}, \varrho_0) \stackrel{\text{Eq. (8)}}{\approx} \epsilon_r^2(P, \mathbf{c}_*). \quad (16)$$

and we calculate the time $t = t_r$ error as

$$\epsilon_r^2(P, \mathbf{c}_*) := \frac{\|(e^{t_r P} \mathbf{c}_* - \mathbf{c}_r)^\top \psi(\cdot)\|_{L^2}^2}{\|\mathbf{c}_*^\top \psi(\mathbf{x})\|_{L^2}^2} = \frac{\|e^{t_r P} \mathbf{c}_* - \mathbf{c}_r\|_M^2}{\|\mathbf{c}_r\|_M^2} = \frac{[e^{t_r P} \mathbf{c}_* - \mathbf{c}_r]^\top M [e^{t_r P} \mathbf{c}_* - \mathbf{c}_r]}{\mathbf{c}_r^\top M \mathbf{c}_r}, \quad (17)$$

where we introduce the mass matrix weighted norm $\|\mathbf{c}\|_M := \sqrt{\mathbf{c}^\top M \mathbf{c}}$. We then choose the loss function

$$\mathcal{L} = \frac{1}{R + 1} \sum_{r=0}^R \epsilon_r^2(P, \mathbf{c}_*). \quad (18)$$

2.2.1 Option 1: Inference of Projected Perron–Frobenius Operator Matrix P [DDD]

We now need to address the issue of how to determine P from data. In order to preserve probability density and positivity, we require $P \in \mathcal{P}$ for

$$\mathcal{P} = \left\{ P \in \mathbb{R}^{N \times N} : \sum_{k=1}^N P_{kj} = 0 \text{ and } P_{ij} \geq 0 \text{ for } i, j = 1, \dots, N \text{ and } i \neq j \right\}. \quad (19)$$

This is motivated by conservation of probability mass, i.e., requiring $d/dt[\|\mathbf{c}(t)\|_1] = 0$ and employing equation (10). DDD then corresponds to finding the solution to a finite dimensional approximation to equation (15), given by

$$\{P, \mathbf{c}_*\} := \arg \min_{P \in \mathcal{P}, \mathbf{c}_* \in \Lambda} \frac{1}{R + 1} \sum_{r=0}^R \epsilon_r^2(P, \mathbf{c}_*). \quad (20)$$

From Taylor-King *et al.* [30], the matrix P and initial condition \mathbf{c}_* with relevant constraints have $(N-1)(N+1) = \mathcal{O}(N^2)$ degrees of freedom. To enable gradient descent, one can calculate the t_r relative error with respect to P as

$$\frac{\partial \varepsilon_r^2}{\partial P} = \frac{2}{\mathbf{c}_r^\top M \mathbf{c}_r} \sum_{k=0}^{\infty} \frac{t^{k+1}}{(k+1)!} \sum_{j=0}^k (P^{k-j})^\top M (e^{t_r P} \mathbf{c}_* - \mathbf{c}_r) \mathbf{c}_*^\top (P^j)^\top \quad (21)$$

$$= \frac{2}{\mathbf{c}_r^\top M \mathbf{c}_r} \sum_{k=0}^{\infty} \frac{t^{k+1}}{(k+1)!} S_k, \quad (22)$$

and the derivative with respect to \mathbf{c}_* as

$$\frac{\partial \varepsilon_r^2}{\partial \mathbf{c}_*} = \frac{2}{\mathbf{c}_r^\top M \mathbf{c}_r} [e^{t_r P}]^\top M [e^{t_r P} \mathbf{c}_* - \mathbf{c}_r]. \quad (23)$$

The terms $S_k = \sum_{j=0}^k (P^{k-j})^\top M (e^{t_r P} \mathbf{c}_* - \mathbf{c}_r) \mathbf{c}_*^\top (P^j)^\top$ can be calculated using the recursion relation

$$S_k = P^\top S_{k-1} + S_{k-1} P^\top - P^\top S_{k-2} P^\top, \quad \text{where} \quad \begin{cases} S_{-1} = \mathbf{0} \\ S_0 = M (e^{t_r P} \mathbf{c}_* - \mathbf{c}_r) \mathbf{c}_*^\top. \end{cases} \quad (24)$$

2.2.2 Option 2: Inference of Matrix Q for Local Differential Operators [Sparse DDD]

Another option is to use compact basis functions (i.e., ψ_i has finite support), then by restricting \mathcal{P} to local differential operators only, M can be made sparse. For the sake of argument, M could have $\mathcal{O}(N \log N)$ non-zero elements; however $P = M^{-1}Q$ would still have $\mathcal{O}(N^2)$ degrees of freedom (because Q is dense). A workaround would be to enforce that \mathcal{P} consists only of *local* differential operators, namely

$$\mathcal{P} = \sum_{|\alpha| \in \mathbb{N}} \sum_{\alpha \in \mathbb{N}_0^d} a_\alpha \frac{\partial^{|\alpha|}}{\partial x_1^{\alpha_1} \dots \partial x_d^{\alpha_d}}, \quad (25)$$

for $a_\alpha \in \mathbb{R}$. For the case of equation (25), whenever the mass matrix is zero, the corresponding entry of Q is also zero:

$$M_{ij} = 0 \implies Q_{ij} = 0. \quad (26)$$

Therefore, DDD can be made sparse by only inferring the non-zero entries of matrix Q , thus Sparse DDD. We then simply change the argument of the minimisation problem, so

$$\{Q, \mathbf{c}_*\} := \arg \min_{Q \in \mathcal{Q}, \mathbf{c}_* \in \Lambda} \frac{1}{R+1} \sum_{r=0}^R \varepsilon_r^2(Q, \mathbf{c}_*). \quad (27)$$

and therefore we can calculate the derivative with respect to Q using the chain rule

$$\frac{\partial \varepsilon_r^2}{\partial Q} = M^{-1} \frac{\partial \varepsilon_r^2}{\partial P}. \quad (28)$$

We then also have to modify equation (19) to choosing

$$\mathcal{Q} = \left\{ Q \in \mathbb{R}^{N \times N} : \sum_{k=1}^N \sum_{l=1}^N M_{kl}^{-1} Q_{lj} = 0 \text{ and } \sum_{l=1}^N M_{il}^{-1} Q_{lj} \geq 0 \text{ for } \begin{matrix} i, j = 1, \dots, N \\ i \neq j \end{matrix} \right\}. \quad (29)$$

2.3 Integrating Trajectory and Snapshot Data

It is simple to calculate a series of coefficients for both the collection of $K_{\mathcal{T}}$ trajectory time series, $\{\mathbf{c}_{r,k}\}_{r=1, k=1}^{R_{\mathcal{T}}, K_{\mathcal{T}}}$, and the snapshot dataset $\{\mathbf{c}_r\}_{r=1}^{R_S}$. We combine loss functions to obtain

$$\frac{\lambda}{K_{\mathcal{T}}(R_{\mathcal{T}}+1)} \sum_{k=0}^{K_{\mathcal{T}}} \sum_{r=0}^{R_{\mathcal{T}}} \varepsilon_{r, \mathcal{T}}^2(P, \mathbf{c}_{k,*}) + \frac{1-\lambda}{R_S+1} \sum_{r=0}^{R_S} \varepsilon_{r, S}^2(P, \mathbf{c}_*). \quad (30)$$

Because the errors from predicting a trajectory will likely be higher (snapshots capture distributions vs. trajectories of delta functions), we introduce a hyperparameter $\lambda \in (0, 1)$.

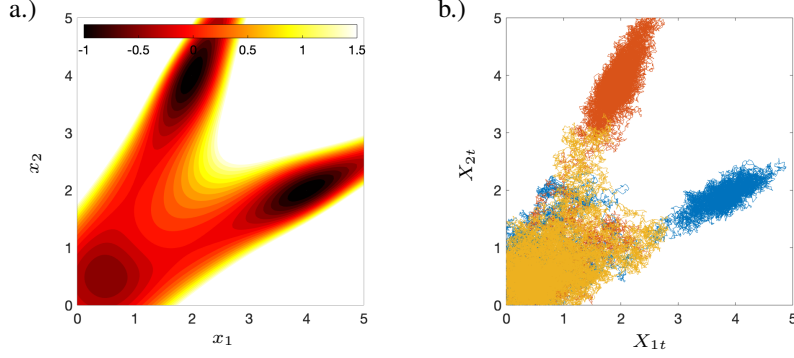


Figure 1: (a.) The potential well from equation (33) is illustrated. (b.) Three sample trajectories are shown from the stochastic dynamical system described by equation (32)–(33).

Finally, as we may be wishing to include many trajectories ($K_{\mathcal{T}} \gg 1$), having unassigned initial conditions for all trajectories will lead to an increase of $K_{\mathcal{T}}N$ parameters. Therefore, we assign the initial condition to the first observation, i.e., $\mathbf{c}_{k,*} = \mathbf{c}_{0,k}$ and therefore $\varepsilon_{0,\mathcal{T}} \equiv 0$, leading to loss function

$$\mathcal{L}_{\text{tot}} = \frac{\lambda}{K_{\mathcal{T}}(R_{\mathcal{T}} + 1)} \sum_{k=1}^{K_{\mathcal{T}}} \sum_{r=1}^{R_{\mathcal{T}}} \varepsilon_{r,\mathcal{T}}^2(P) + \frac{1 - \lambda}{R_{\mathcal{S}} + 1} \sum_{r=0}^{R_{\mathcal{S}}} \varepsilon_{r,\mathcal{S}}^2(P, \mathbf{c}_*). \quad (31)$$

3 Experiments

3.1 Simulated Data Generation

For this worked example, we take the stochastic differential equation from Taylor-King *et al.* [30]. We consider point particles in a bistable potential well undergoing Brownian fluctuations. After initialisation around point $(1, 1)^{\top}/2$, particles may switch between bistable paths along lines: $y = 2x$ or $y = x/2$ to finally settle in one of the two final state $(2, 4)^{\top}$ or $(4, 2)^{\top}$. The process is described by two-dimensional SDE $\{\mathbf{X}_t = (X_{1t}, X_{2t})^{\top} \in \mathbb{R}_+^2 : t \geq 0\}$

$$d\mathbf{X}_t = -\nabla V(\mathbf{X}_t)dt + \sqrt{2D} d\mathbf{W}_t, \quad (32)$$

where \mathbf{W}_t is a two-dimensional Wiener process and the potential well is plotted in Figure 1(a) and is given by

$$V(\mathbf{x}) = \left(\frac{1}{2} [\|\mathbf{x}\|^2 - x_1 x_2] - \frac{1}{10} \|\mathbf{x}\|^2 \right)^2 - \frac{1}{2} e^{-\frac{1}{2} \|\mathbf{x} - (\frac{1}{2}, \frac{1}{2})^{\top}\|^2} - e^{-\|\mathbf{x} - (4, 2)^{\top}\|^2} - e^{-\|\mathbf{x} - (2, 4)^{\top}\|^2}. \quad (33)$$

As an initial condition at $t_0 = 0$, the sample is placed with a multivariate normal distribution with mean $\boldsymbol{\mu} = (1, 1)^{\top}/2$ and covariance matrix $\Sigma = \text{diag}(0.5, 0.5)$. Three sample trajectories are visualised using an Euler–Maruyama with time step $\delta t = 2^{-9}$, see Figure 1(b); the diffusion constant is chosen to be $D = 1/4$. Along the lines $x = 0$ and $y = 0$, the system has reflecting boundary conditions.

3.1.1 Datasets Generated

To limit the introduction of sampling errors, all datasets are subsets of a parent dataset whereby 1000 trajectories generated by the SDE described by equation (32)–(33) are observed at time points $t = 0, 1, 2, 3, 5, 8, 13, 21, 34, 55$ and 89.

Trajectory Dataset For this dataset, 100 samples are randomly taken at the 11 timepoints listed above. As one can imagine, the early trajectories with small gaps between observations contain the most relevant information.

Full Snapshot Dataset Here, all 1000 samples are used. Of course, continuous trajectories are not used — therefore for the samples associated to a fixed timepoint, index permutation does not change the results.

Two Snapshot Dataset A reduced snapshot dataset is created by taking the first and fourth snapshot. Most of the fast dynamics have taken place by this point in time.

Integrated Dataset A composite dataset is created by taking both the Two Snapshot Dataset and 10 of the 100 samples from the Trajectory Dataset.

3.2 Basis Functions Selection

For Sparse DDD, we require compact local basis functions. For simplicity, we use radial piecewise linear basis functions

$$\psi_j(\mathbf{x}) = \frac{d(d+1)\Gamma(\frac{d}{2})}{2\pi^{d/2}\zeta_j^d} \begin{cases} 1 - \frac{\|\mathbf{x}-\mathbf{x}_j\|}{\zeta_j} & \text{for } \|\mathbf{x}-\mathbf{x}_j\| < \zeta_j \\ 0 & \text{otherwise.} \end{cases} \quad (34)$$

We select the values of $\{\mathbf{x}_j\}_{j=1}^N$ using k -means clustering with $k = 30$ over the Full Snapshot Dataset. The values of ζ_j are chosen such that the support of each basis function covers the centers of the 2 nearest basis functions.

Mass Matrix Calculation

The mass matrix is given by

$$M_{ij} = \langle \psi_i, \psi_j \rangle_\mu = \int_{\mathcal{M}} \psi_i(\mathbf{x})\psi_j(\mathbf{x}) d\mu(\mathbf{x}). \quad (35)$$

Typically in the Dynamic Mode Decomposition field, one would use a data driven measure $\mu_D(\mathbf{x}) = \sum_{l=1}^L \delta(\mathbf{x} - \mathbf{x}_l)/L$ and then M_{ij} is calculated as

$$M_{ij} = \int_{\mathcal{M}} \psi_i(\mathbf{x})\psi_j(\mathbf{x}) d\mu_D(\mathbf{x}) = \frac{1}{L} \sum_{l=1}^L \psi_i(\mathbf{x}_l)\psi_j(\mathbf{x}_l). \quad (36)$$

However, for a combination of snapshot and trajectory data one may have different numbers of data points k_r at each time point t_r . This may complicate the use of a data driven measure. Therefore, we integrate equation (35) as a Riemann integral. As analytical expressions for many choices in basis functions are seldom known for equation (35), we use Monte Carlo integration

$$M_{ij} = \int_{\mathcal{M}} \psi_i(\mathbf{x})\psi_j(\mathbf{x}) d\mathbf{x} \approx \frac{|\Omega|}{L} \sum_{l=1}^L \psi_i(\mathbf{x}_l)\psi_j(\mathbf{x}_l), \quad (37)$$

whereby \mathbf{x}_l is sampled uniformly at random from $\Omega \subset \mathbb{R}^d$. We choose Ω as a d -dimensional hypercube to enclose the support of one of the basis functions. Superior convergence of equation (37) is achieved via quasi-Monte Carlo integration with Halton node placing [20].

3.3 Comparison between DDD and Sparse DDD

To prevent numerical instability for large times, we re-scale the experimental time course (t_1, t_R) to the unit interval. We then run DDD (Section 2.2.1) and Sparse DDD (Section 2.2.2) on the 4 datasets created in Section 3.1.1 using sequential quadratic programming (SQP).

For the $N = 30$ basis functions, DDD has $N^2 = 900$ parameters or $N(N - 1) = 870$ degrees of freedom (columns of P summing to zero). However, after fixing the corresponding zero-valued indices of M to zero in Q , Sparse DDD has 220 parameters, or 190 degrees of freedom. As one would expect, Sparse DDD is computationally much faster than DDD.

In Table 1, we show the mean relative error for the test Full Snapshot Dataset — but trained separately on the 4 individual datasets. We find that, apart from the Trajectory Dataset, DDD always achieves a

Table 1: Mean relative error for Sparse DDD and DDD applied to the 4 datasets from Section 3.1.1 and tested on the Full Snapshot Dataset.

Dataset	Mean relative error	
	Sparse DDD	DDD
Trajectory	0.760	0.811
Full Snapshot	0.079	0.053
Two Snapshot	0.360	0.303
Integrated	0.291	0.239

marginally lower error. We also plot the log percentage relative predictive error at each time point in Figure 2.

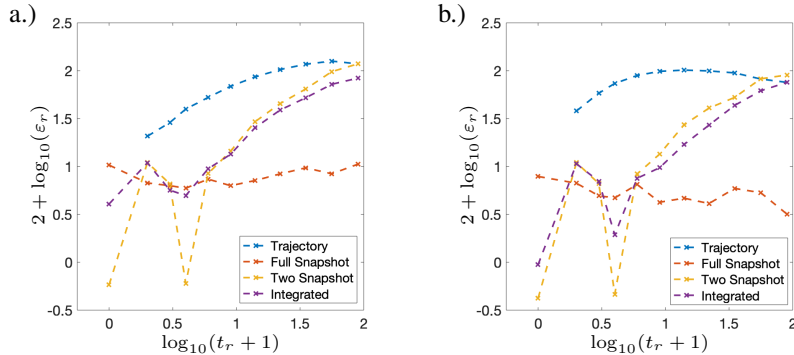


Figure 2: Relative prediction error for the Full Snapshot dataset at each time point for: (a.) Sparse DDD, and (b.) DDD.

Examining Figure 2, we find that:

- The Trajectory Dataset has consistently high error, but this is for two reasons: (1) due to the large time gaps between observations, 100 trajectories does not contain a huge amount of information to infer a Markov transition rate matrix; and (2) as explained in Section 2.3, initial conditions for time series are not left as a free parameter. For evaluation of the test set, we fix the initial condition as $c_* = c_0$.
- The Full Snapshot Dataset achieves consistently low fitting error. Note that for this problem, the training and test set are identical.
- The Two Snapshot Dataset achieves very low error around the specified two time points, but error quickly increases for later time points.
- By incorporating 10 trajectories, the Integrated Dataset achieves better error at later time points than the Two Snapshot Dataset. For the free hyperparameter from Section 2.3, we choose $\lambda = 0.01$.

Taking these observations together, we show that information from trajectory and snapshot time series data can be combined to provide better fits than either datasets individually.

4 Discussion and Conclusion

We have presented an approach for synergistic integration of trajectory and snapshot time series datasets. We believe that data integration of this form will become increasingly relevant as we wish to: (1) integrate different patient datasets (static vs. longitudinal cohorts) and (2) integrate various modalities of cell profiling, such as live cell imaging with accompanied multi-omics. A key future challenge will be methods designed with incomplete observations using different measurements, for example, single cell RNA-seq ($\sim 20,000$ mRNA transcripts) and flow/mass cytometry ($\sim 5-50$ surface proteins).

The numerical approximation of operators is an emerging field and therefore approaches are still being optimised and refined. A hurdle practitioners often face is the selection of basis functions that well characterise the time series data; many options are available, including radial basis functions [9] and global basis functions [14]. Greater numbers of basis functions alleviate the problem of data better data representation at the cost of more parameters to be inferred. Sparse methods have therefore been proposed for DMD in a discrete time setting [7, 13, 12], but Sparse DDD appears to be a first attempt in a continuous-time setting.

Acknowledgments and Disclosure of Funding

We gratefully acknowledge the help of Tomislav Plesa, Asbjorn Riseth and Manfred Claassen.

This work has been wholly supported by Relation Therapeutics Limited.

References

- [1] Aldridge, B. B., Burke, J. M., Lauffenburger, D. A., and Sorger, P. K. (2006). Physicochemical modelling of cell signalling pathways. *Nature cell biology*, **8**(11), 1195.
- [2] Beaulieu-Jones, B. K., Orzechowski, P., and Moore, J. H. (2018). Mapping patient trajectories using longitudinal extraction and deep learning in the mimic-iii critical care database. In *PSB*, pages 123–132. World Scientific.
- [3] Cannoodt, R., Saelens, W., and Saeys, Y. (2016). Computational methods for trajectory inference from single-cell transcriptomics. *European journal of immunology*, **46**(11), 2496–2506.
- [4] Chen, Z., Leskelä, L., and Viitasaari, L. (2019). Pathwise stieljes integrals of discontinuously evaluated stochastic processes. *Stochastic Processes and their Applications*, **129**(8), 2723–2757.
- [5] Ching, T., Himmelstein, D. S., Beaulieu-Jones, B. K., Kalinin, A. A., Do, B. T., Way, G. P., Ferrero, E., Agapow, P.-M., Zietz, M., Hoffman, M. M., *et al.* (2018). Opportunities and obstacles for deep learning in biology and medicine. *Journal of The Royal Society Interface*, **15**(141), 20170387.
- [6] de Haan-Rietdijk, S., Voelkle, M. C., Keijsers, L., and Hamaker, E. L. (2017). Discrete-vs. continuous-time modeling of unequally spaced experience sampling method data. *Frontiers in Psychology*, **8**, 1849.
- [7] Dicle, C., Mansour, H., Tian, D., Benosman, M., and Vetro, A. (2016). Robust low rank dynamic mode decomposition for compressed domain crowd and traffic flow analysis. In *2016 IEEE International Conference on Multimedia and Expo (ICME)*, pages 1–6. IEEE.
- [8] Duan, J. A., Gelfand, A. E., Sirmans, C., *et al.* (2009). Modeling space-time data using stochastic differential equations. *Bayesian analysis*, **4**(4), 733–758.
- [9] Fornberg, B. and Flyer, N. (2015). *A primer on radial basis functions with applications to the geosciences*. SIAM.
- [10] Gilbarg, D. and Trudinger, N. S. (2015). *Elliptic partial differential equations of second order*. Springer.
- [11] Hashimoto, T., Gifford, D., and Jaakkola, T. (2016). Learning population-level diffusions with generative recurrent networks. In *International Conference on Machine Learning*, pages 2417–2426.
- [12] Héas, P. and Herzet, C. (2017). Optimal low-rank dynamic mode decomposition. In *2017 IEEE International Conference on Acoustics, Speech and Signal Processing (ICASSP)*, pages 4456–4460.
- [13] Kaneko, Y., Muramatsu, S., Yasuda, H., Hayasaka, K., Otake, Y., Ono, S., and Yukawa, M. (2019). Convolutional-sparse-coded dynamic mode decomposition and its application to river state estimation. In *ICASSP 2019-2019 IEEE International Conference on Acoustics, Speech and Signal Processing (ICASSP)*, pages 1872–1876. IEEE.
- [14] Klus, S., Koltai, P., and Schütte, C. (2016). On the numerical approximation of the Perron-Frobenius and Koopman operator. *Journal of Computational Dynamics*, **3**(1), 51–79.
- [15] Klus, S., Nüske, F., Koltai, P., Wu, H., Kevrekidis, I., Schütte, C., and Noé, F. (2017). Data-driven model reduction and transfer operator approximation. *arXiv preprint arXiv:1703.10112*.

- [16] Klus, S., Gelß, P., Peitz, S., and Schütte, C. (2018). Tensor-based dynamic mode decomposition. *Nonlinearity*, **31**(7), 3359.
- [17] Klus, S., Nüske, F., Peitz, S., Niemann, J.-H., Clementi, C., and Schütte, C. (2020). Data-driven approximation of the koopman generator: Model reduction, system identification, and control. *Physica D: Nonlinear Phenomena*, **406**, 132416.
- [18] Mariani, M. C. and Tweneboah, O. K. (2016). Stochastic differential equations applied to the study of geophysical and financial time series. *Physica A: Statistical Mechanics and its Applications*, **443**, 170–178.
- [19] Mauroy, A. and Goncalves, J. (2017). Koopman-based lifting techniques for nonlinear systems identification. *arXiv e-prints*.
- [20] Morokoff, W. J. and Caffisch, R. E. (1995). Quasi-monte carlo integration. *Journal of computational physics*, **122**(2), 218–230.
- [21] Riseth, A. N. and Taylor-King, J. P. (2017). Operator Fitting for Parameter Estimation of Stochastic Differential Equations. *arXiv e-prints*.
- [22] Rubanova, Y., Chen, T. Q., and Duvenaud, D. K. (2019). Latent ordinary differential equations for irregularly-sampled time series. In *Advances in Neural Information Processing Systems*, pages 5321–5331.
- [23] Saelens, W., Cannoodt, R., Todorov, H., and Saeys, Y. (2018). A comparison of single-cell trajectory inference methods: towards more accurate and robust tools. *bioRxiv*.
- [24] Schiebinger, G., Shu, J., Tabaka, M., Cleary, B., Subramanian, V., Solomon, A., Liu, S., Lin, S., Berube, P., Lee, L., Chen, J., Brumbaugh, J., Rigollet, P., Hochedlinger, K., Jaenisch, R., Regev, A., and Lander, E. (2017). Reconstruction of developmental landscapes by optimal-transport analysis of single-cell gene expression sheds light on cellular reprogramming. *bioRxiv*.
- [25] Schmid, P. J. (2010). Dynamic mode decomposition of numerical and experimental data. *Journal of fluid mechanics*, **656**, 5–28.
- [26] Schmid, P. J., Li, L., Juniper, M. P., and Pust, O. (2011). Applications of the dynamic mode decomposition. *Theoretical and Computational Fluid Dynamics*, **25**(1-4), 249–259.
- [27] Setty, M., Tadmor, M. D., Reich-Zeliger, S., Angel, O., Salame, T. M., Kathail, P., Choi, K., Bendall, S., Friedman, N., and Pe’er, D. (2016). Wishbone identifies bifurcating developmental trajectories from single-cell data. *Nature biotechnology*, **34**(6), 637.
- [28] Siddiqi, H. K. and Mehra, M. R. (2020). Covid-19 illness in native and immunosuppressed states: a clinical-therapeutic staging proposal. *The Journal of Heart and Lung Transplantation*.
- [29] Sungnak, W., Huang, N., Bécavin, C., Berg, M., Queen, R., Litvinukova, M., Talavera-López, C., Maatz, H., Reichart, D., Sampaziotis, F., *et al.* (2020). Sars-cov-2 entry factors are highly expressed in nasal epithelial cells together with innate immune genes. *Nature medicine*, pages 1–7.
- [30] Taylor-King, J. P., Riseth, A. N., Macnair, W., and Claassen, M. (2020). Dynamic distribution decomposition for single-cell snapshot time series identifies subpopulations and trajectories during ipsc reprogramming. *PLOS Computational Biology*, **16**(1), e1007491.
- [31] Tu, J. H., Rowley, C. W., Luchtenburg, D. M., Brunton, S. L., and Kutz, J. N. (2013). On dynamic mode decomposition: Theory and applications. *arXiv preprint arXiv:1312.0041*.
- [32] Weinreb, C., Wolock, S., Tusi, B. K., Socolovsky, M., and Klein, A. M. (2018). Fundamental limits on dynamic inference from single-cell snapshots. *Proceedings of the National Academy of Sciences*, **115**(10), E2467–E2476.
- [33] Williams, M. O., Kevrekidis, I. G., and Rowley, C. W. (2015). A data-driven approximation of the Koopman operator: Extending dynamic mode decomposition. *Journal of Nonlinear Science*, **25**(6), 1307–1346.
- [34] Yang, B. and Bao, W. (2019). Complex-valued ordinary differential equation modeling for time series identification. *IEEE Access*, **7**, 41033–41042.
- [35] Zechner, C., Ruess, J., Krenn, P., Pelet, S., Peter, M., Lygeros, J., and Koepl, H. (2012). Moment-based inference predicts bimodality in transient gene expression. *Proceedings of the National Academy of Sciences*, **109**(21), 8340–8345.

- [36] Zhao, Y., Qin, L., Zhang, P., Li, K., Liang, L., Sun, J., Xu, B., Dai, Y., Li, X., Zhang, C., *et al.* (2020). Longitudinal profiling of cytokines and chemokines in covid-19 reveals inhibitory mediators il-1ra and il-10 are associated with disease severity while elevated rantes is an early predictor of mild disease. *The Lancet*.
- [37] Ziemer, W. P. (2012). *Weakly differentiable functions: Sobolev spaces and functions of bounded variation*, volume 120. Springer Science & Business Media.
- [38] Zunder, E. R., Lujan, E., Goltsev, Y., Wernig, M., and Nolan, G. P. (2015). A continuous molecular roadmap to ipsc reprogramming through progression analysis of single-cell mass cytometry. *Cell Stem Cell*, **16**(3), 323–337.